Check for updates

MATERIALS SCIENCE

Boosting capacitive energy storage in relaxor ferroelectrics through polymorphic phase engineering

Yang Zhang[1,2]†, Huan Liang[1]†, Yajing Liu[1], Dong Li[1], Shuai Dong[2], Jing Wang[3]*, Weiwei Li[1,4]*, Ce-Wen Nan[5]

Copyright © 2026 The Authors, some rights reserved; exclusive licensee American Association for the Advancement of Science. No claim to original U.S. Government Works. Distributed under a Creative Commons Attribution NonCommercial License 4.0 (CC BY-NC).

Relaxor ferroelectric materials are promising for next-generation capacitors due to their high energy storage capacity. Polymorphic phase engineering, where different ferroelectric phases coexist, has been widely demonstrated as an effective approach to further boost capacitive energy storage performance of relaxor ferroelectrics, but the reasons for these improvements and how they compare to single-phase systems remain unclear. Here, taking dendrite-like $PbZr_{1-x}Ti_xO_3$/MgO nanocomposites with defected as a model system, we systematically examine properties and capacitive energy storage performance for rhombohedral-dominant, rhombohedral/tetragonal-mixed, and tetragonal-dominant phases through phase-field simulations. We find that the rhombohedral/tetragonal mixtures deliver the best results in most cases, mainly due to their low switching barriers and substantial local inhomogeneity. These results offer a detailed view of improved energy storage in relaxor ferroelectrics and provide theoretical guidance for designing high-performance capacitors.

INTRODUCTION

Electrostatic capacitors based on dielectrics are strong candidates for next-generation pulsed-power and high-power energy storage systems, thanks to their ultrafast charge/discharge speeds and superior stability (*1*–*5*). However, their relatively low energy density limits further miniaturization and integration into electronic and electrical devices (*6*). Typically, the charged energy density (U_c) and the dischargeable energy density (U_e) of a capacitor are derived from its polarization-electric field (*P*-*E*) hysteresis loop as $U_c = \int_{-P_r}^{P_m} E dP$ and $U_e = -\int_{P_m}^{P_r} E dP$, where P_m is the maximum polarization and P_r is the remnant polarization. The efficiency (η) is then $\eta = U_e/U_c \times 100\%$. Thus, achieving high U_e and η requires not only strong electrical breakdown strength (E_b) but also large P_m and small P_r—in other words, a substantial reversible polarization ($\Delta P = P_m - P_r$).

Dielectric materials based on ferroelectric (FE) oxides show potential for energy storage applications due to their high maximum polarization P_m, but their typically large remnant polarization P_r and low breakdown strength E_b constrain performance (*3*, *7*). To address these limitations, one key strategy is to transform conventional FEs into more disordered versions known as relaxor FEs (RFEs). This involves introducing local inhomogeneity (*8*, *9*) and breaking up large, organized domains, which result in polar nanoregions (PNRs) or polar slushes (*4*, *10*–*13*). The nanoscale features respond readily and independently to external electric fields because the switching barrier is lower after removing long-range FE interactions, leading to slim *P*-*E* loops. Common techniques include chemical modifications (*4*, *14*, *15*), defect engineering (*16*–*18*), and interface design (*19*–*23*). For instance, solid solutions or doping can generate PNRs embedded in a nonpolarized matrix (*4*, *24*, *25*). Similarly, high-entropy engineering incorporate multiple elements to increase local electrical and elastic disorder, thus shrinking domain sizes (*14*, *15*, *26*–*28*). In addition, defects, such as point defects and defect dipoles created via ion bombardment or in situ–controlled oxygen environments, can trap and stabilize local polarizations and weaken overall ordered polarizations (*16*, *17*, *29*). At optimal levels, these modified materials enhance performance over pristine ones. Meanwhile, nanocomposites combining FEs with linear dielectrics reduce the size of polarized region and block dielectric breakdown paths (*20*, *22*, *30*), thereby lowering P_r while raising E_b; here, the nonpolar materials could be wide-bandgap insulators (*21*) or grain boundaries (*12*, *27*, *31*).

Building on these relaxor strategies, an established method to further reduce the energy needed for switching is through polymorphic phase engineering, where domains with different symmetries like rhombohedral (R, with ⟨111⟩-oriented polarizations) and tetragonal (T, with ⟨100⟩-oriented polarizations) coexist (*4*, *14*). A well-known example is the morphotropic phase boundaries (MPBs) in FE materials such as $PbZr_{1-x}Ti_xO_3$ (PZT), $(K,Na)NbO_3$ (KNN), and $Pb(Mg,Nb)O_3$-$PbTiO_3$ (PMN-PT), which greatly improves piezoelectric responses (*32*–*35*). For PZT, as shown in its phase diagram (fig. S1), R/T-mixed regions may appear near MPB at Ti content $x \sim 50\%$. Figure 1A illustrates domain structures and corresponding *P*-*E* loops for PZT with $x = 30\%$ (R dominant), 50% (R/T mixed), and 70% (T dominant). The R phase exhibits moderate coercive fields and lower saturation polarization because it always has components perpendicular to applied electric fields. The T phase has higher coercive fields and greater polarization, as it can align completely with the field. The R/T-mixed phase yields the lowest coercive field due to low switching barriers and high saturation polarization from easy interphase switching (fig. S2).

It is natural to find that combining relaxor features with polymorphic phases can further minimize energy barriers and thus improve energy storage performance. This has been demonstrated in systems like $BiFeO_3$-$BaTiO_3$-$SrTiO_3$ solid solutions (*4*) and multidoped high-entropy $BaTiO_3$–based ceramics (*14*), in which polymorphic PNRs

[1]College of Physics, MIIT Key Laboratory of Aerospace Information Materials and Physics, State Key Laboratory of Mechanics and Control for Aerospace Structures, Nanjing University of Aeronautics and Astronautics, Nanjing 211106, China. [2]Key Laboratory of Quantum Materials and Devices of Ministry of Education, School of Physics, Southeast University, Nanjing 211189, China. [3]State Key Laboratory of Mechanics and Control for Aerospace Structures, College of Aerospace Engineering, Nanjing University of Aeronautics and Astronautics, Nanjing 210016, China. [4]College of Integrated Circuits, MIIT Key Laboratory of Aerospace Integrated Circuits and Microsystem, Nanjing University of Aeronautics and Astronautics, Nanjing 211106, China. [5]State Key Laboratory of New Ceramics and Fine Processing, School of Materials Science and Engineering, Tsinghua University, Beijing 100084, China.
*Corresponding author. Email: wang-jing@nuaa.edu.cn (J.W.); wl337@nuaa.edu.cn (W.L.)
†These authors contribute equally to this work.

Downloaded from https://www.science.org on February 20, 2026

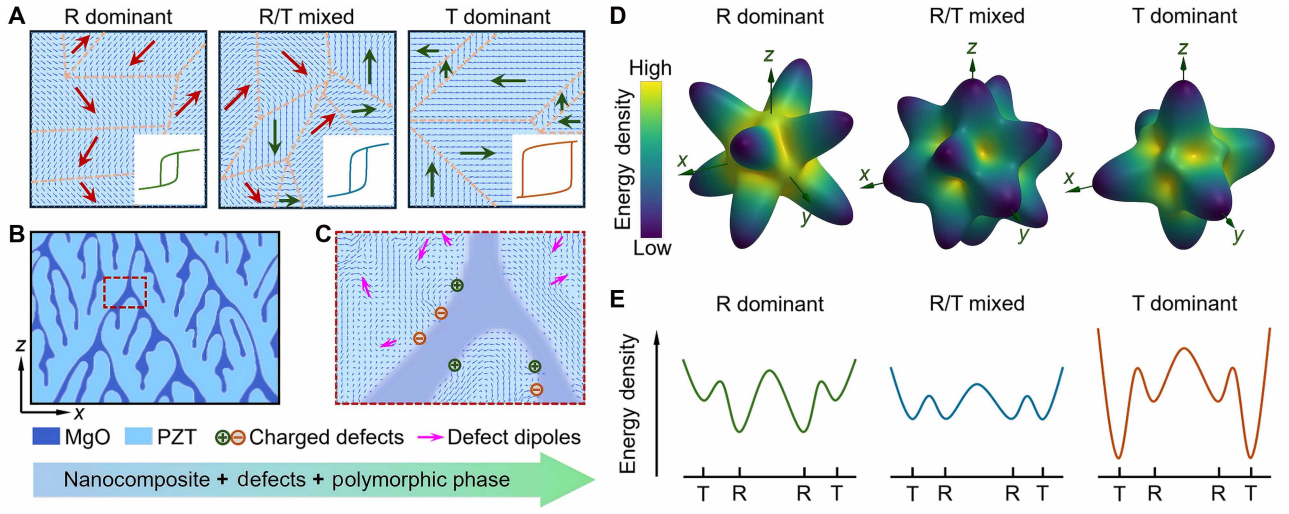

Fig. 1. Design of dendrite-like nanocomposite structure with defect engineering and polymorphic phase strategy. (**A**) Comparison of domain patterns and *P-E* loops for R-dominant, R/T-mixed, and T-dominant phases in PZT, with Ti content x = 30, 50, and 70, respectively. (**B**) Illustration of a dendrite-like PM nanocomposite structure. (**C**) Simulated domain structures with charged defects and defect dipoles. The displayed area is 18 nm by 12 nm, enlarged from dashed red square in (B). (**D** and **E**) Comparison of (D) three-dimensional energy density landscapes and (E) schematic energy profiles for R-dominant, R/T-mixed, and T-dominant phases. The peaks in (D) refer to the lowest energy density of corresponding directions for easier observations.

with R/T-mixed nanodomains form, further enhancing storage capabilities. Likewise, isolated polar slush states in $Bi(Mg,Ti)O_3$-$BaTiO_3$-TiO_2 films display R/orthorhombic (O) and T nanodomains in the polar matrix, integrated with nonpolar boundaries and point defects (*12*). Despite these benefits from polymorphic phases, especially R/T mixtures, the underlying mechanisms, e.g., how the ratios of R/T phases affect dielectric properties and how they interact with nanostructures or defects, are not fully understood.

Recently, a unique dendrite-like FE/dielectric nanocomposite has shown an excellent potential for improving energy storage performance and stability (*18*, *21*). In these $PbZr_{0.53}Ti_{0.47}O_3$/MgO nanocomposites (Fig. 1B), numerous tilted interfaces effectively break larger domains into nanoscale ones while preserving FE continuity, extend breakdown paths, and accommodate defects, thereby reducing P_r, maintaining P_m, enhancing E_b, and further improving radiation tolerance. These result in exceptionally high energy density ($U_e = 215.8$ J cm^{-3}) and good efficiency ($\eta = 80.7\%$). Notably, microstructure images and chemical element proportions suggest the presence of vacancies (*21*), and PZT allows easy adjustment of R/T phases by changing compositions, making it an ideal platform to explore morphotropic phase effects alongside nanocomposites and defects.

Given experimental complexities, this study uses phase-field simulations to examine polymorphic phases and defects in dendrite-like PZT/MgO (PM) nanocomposites. Phase-field modeling can effectively capture domain dynamics and thermodynamical properties in FEs, including energy storage in various capacitor designs (*36*–*39*). Here, dendrite-like structures vary with PZT molar fraction f (Fig. 1B and fig. S3). Charged defects and defect dipoles are then introduced, both disturbing domain patterns and fixing polarizations nearby (Fig. 1C). We also adjust the Ti content x in PZT to induce R-dominant, T-dominant, or R/T-mixed domains (Fig. 1D). The schematic energy profiles (Fig. 1E) indicate that the T-dominant phase has stronger energy barriers, while the mixed phase has lower barriers for easier domain switching. Through simulations varying c, f, and x, we seek to reveal the roles of nanostructures and defects in the formation of nanodomains and validate improvements in energy storage performance via polymorphic phase engineering. To evaluate the universality of our findings beyond this biphasic model, we also performed supplementary simulations on a doped (Bi,Na)TiO_3 (BNT)-based single-phase system with defect engineering, which confirmed consistent trends in polymorphic effects. This work aims to determine the impact of polymorphic phases on energy storage performance and provide guidance for developing advanced electrostatic capacitors.

RESULTS

Effects of defects and dendrite-like nanostructures

We first examined the effect of defects in the dendrite-like PM nanocomposites. On the basis of previous experiments, it is reasonable to assume the presence of oxygen vacancies and cation vacancies, particularly involving lead (*21*, *29*). These vacancies tend to stabilize at FE/dielectric interfaces due to large differences in lattice properties, forming charged point defects that create local electric fields and contribute to polarization discontinuities. In contrast, within FE regions, these shallow-level defects prefer to pair and form neutral defect dipoles so as to deepen energy states (*17*), which are relatively stable and help pin local polarizations. Accordingly, we modeled defects at varying c, assuming that half are charged point defects at the interfaces and half are pinned defect dipoles inside FE parts (see Materials and Methods).

For simplicity, we chose a PM system with PZT molar fraction of $f = 50\%$ and Ti content of $x = 50\%$ (near MPBs). All simulated domain structures exhibit coexistence of R and T phases (Fig. 2A and fig. S4). As shown in Fig. 2A (left), even without defects, the average domain size remains nanoscale (~3.3 nm; Fig. 2B) because the dendrite-like branches are inherently narrow (<10 nm). Furthermore, the FE/dielectric interfaces align polarizations parallel to them to minimize depolarization fields, and differences in lattice constants generate strain discontinuity, leading to substantial electrical and

Downloaded from https://www.science.org on February 20, 2026

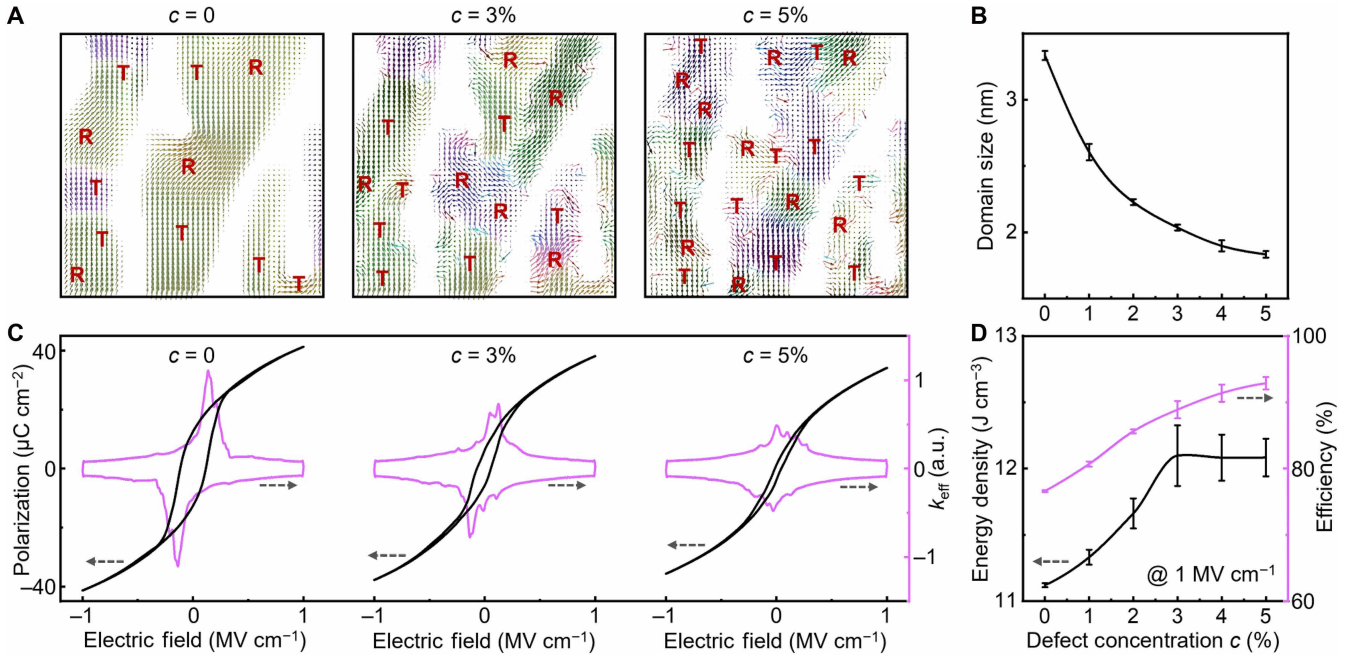

Fig. 2. Domain structures and energy storage performances at varying defect concentrations. (**A**) Domain structures in the PM system with R/T mixtures at PZT molar fraction $f = 50\%$ and Ti content $x = 50\%$ for defect concentrations $c = 0$, 3, and 5%. The displayed area is 20 nm by 20 nm. (**B**) Average domain sizes as a function of defect concentrations. For details on the domain size calculation methodology, see note S1. (**C**) *P-E* loops and effective dielectric constant k_{eff} curves at an electric field of 1 MV cm^{-1} for $c = 0$, 3, and 5%. (**D**) Energy density and efficiency as a function of defect concentrations.

elastic inhomogeneities. Similar effects occur in other systems combining polar and nonpolar materials, such as PNR models in solid solutions or polycrystalline ceramics (*9*). However, these defect-free patterns remain fairly regular, featuring straight domain walls. Introducing randomly distributed defects then disrupts them, transforming the domain structures into a more disordered state (Fig. 2A, middle and right). This occurs because charged defects create strong local electric fields directed toward or away from them, and defect dipoles encourage nearby polarizations to align parallel to reduce gradient energy. As a result, domain sizes decrease further with defects, dropping below 2 nm for $c > 3\%$ (Fig. 2B).

Energy storage properties depend heavily on these domain patterns. For the pristine PM system without defects, the *P-E* loop is already slimmer than that of pure PZT (Fig. 3C, left), leading to an energy density U_e exceeding 11 J cm^{-3} and an efficiency η of ~77% at an electric field of 1 MV cm^{-1} (Fig. 2D). In addition, the curve of effective dielectric constant (k_{eff}, calculated as the differential of polarization with field dP/dE) displays four peaks rather than two typical peaks of classical FEs (Fig. 2C, left), reflecting delayed and unsynchronized switching caused by interfaces. This suggests that the dendrite-like architecture alone can reduce the remnant polarization P_r compared to pure PZT, thereby generating relaxor characteristics and enhancing overall performance. Clearly, adding defects further reduces P_r, steadily raising U_e and η. They also increase disorders in interactions among nanodomains, yielding extra peaks in k_{eff} curves and even narrower *P-E* loops (Fig. 2C). Note that the pinched loops near zero field for higher c also boosts performance (Fig. 2C, right), akin to antiferroelectric-like behavior (*21*). Moreover, according to experiments, the introduction of defect dipoles not only enhances U_e and η but also suppresses current leakage and elevates the electric breakdown strength E_b (*16*, *17*).

However, as more polarizations become fixed, fewer can align with the applied field, causing the maximum polarization P_m to decline. Therefore, at higher defect level, such as $c > 3\%$, U_e levels off at ~12 J cm^{-3} instead of continuing to rise (Fig. 2D), mirroring the degradation in overdosed materials (*16*, *18*). Meanwhile, our phase-field model excludes leakage currents or related issues, which would likely overestimate outcomes at excessive defect concentrations. To align with experimental findings (*18*, *21*), we thus selected this optimal $c = 3\%$ as a baseline for subsequent analyses of PZT molar fraction f and Ti content x. While c may interact with f and x in practice, fixing c allows us to isolate their effects without altering our main conclusions.

To examine the effects of nanostructures and defects from a thermodynamic perspective, we further calculated the four energy density terms, i.e., Landau free energy, gradient energy, elastic energy, and electrostatic energy, as a function of applied electric fields at $c = 3\%$, $f = 50\%$, and $x = 50\%$ (fig. S5). As fields increase, the elastic and gradient energies remain nearly constant, while the Landau free energy rises slightly because of the polarizations departing from their equilibrium states to align with the fields. Notably, electrostatic energy decreases substantially, driven by the negative contribution $-P_z \cdot E_z$, where P_z is the polarization component parallel to applied electric field component E_z.

The electrostatic spatial distributions highlight the benefits of the dendrite-like structures. At zero field (fig. S6A), polarization vectors rotate in response to defects and interfaces to minimize bound charges, yielding flat internal field and electrostatic energy distributions with minor defect-induced fluctuations. At $E_z = 1$ MV cm^{-1} (fig. S6B), internal fields peak near the titled PM interfaces, where polarization discontinuities create depolarization fields that lower local electrostatic energies. Upon external field removal, these depolarization

Downloaded from https://www.science.org on February 20, 2026

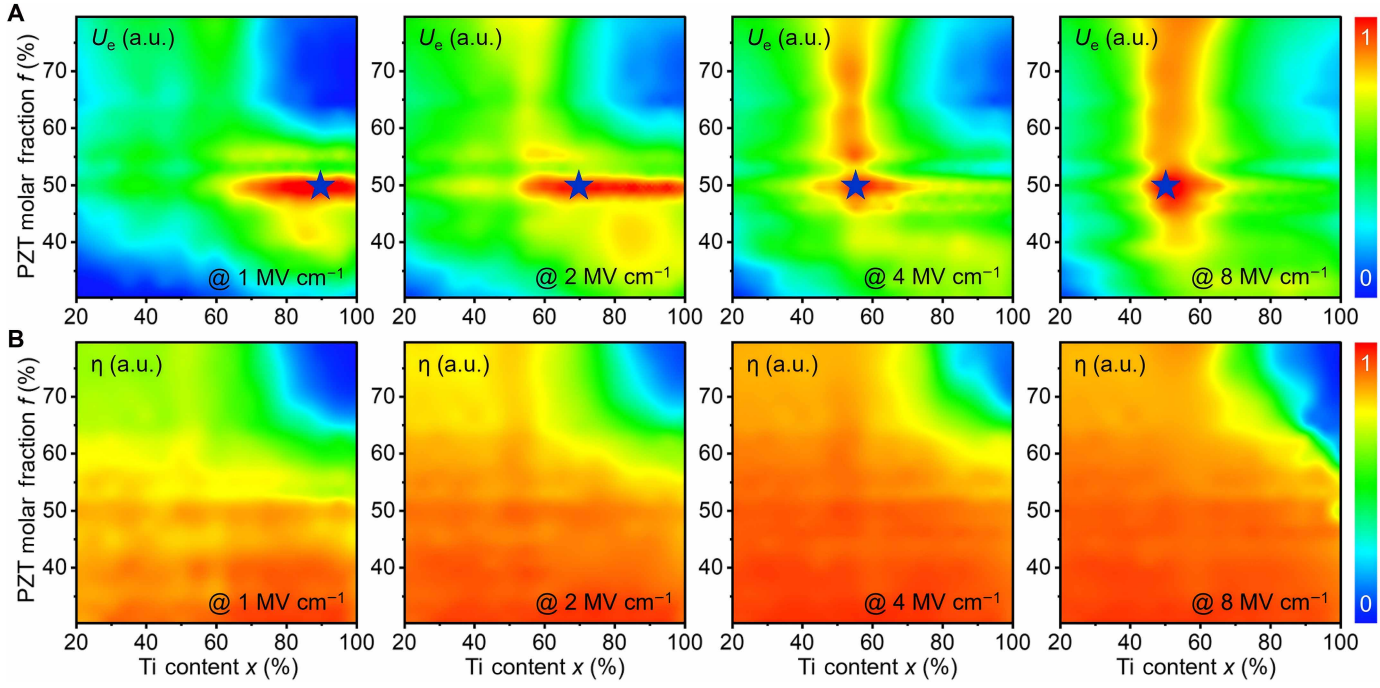

Fig. 3. Maps of energy storage performance in PM systems with respect to Ti contents and PZT molar fractions. (**A** and **B**) Maps of (A) energy density and (B) efficiency at electric fields of 1, 2, 4, and 8 MV cm^{-1}. The stars in (A) mark the optimal points.

fields help revert polarizations to their original states, thus reducing P_r and enhancing relaxor characteristics.

Effects of polymorphic phases

Building on our understanding of how dendrite-like nanostructures and defects convert standard FEs into relaxor versions, we next evaluated energy storage properties by varying PZT molar fraction f and Ti content x. We generated a series of dendrite-like PM structures at various f (fig. S3) using a dendritic growth phase-field model (*40*) and adjusted PZT materials with varying x by changing energy potential coefficients in the simulations (see Materials and Methods). Figure 3 presents contour plots of energy density U_e and efficiency η at applied electric fields of 1, 2, 4, and 8 MV cm^{-1}. Clearly, both f and x substantially influence performance, with field-dependent trends emerging. For f, the peak U_e consistently appears at $f = 50\%$ (Fig. 3A), matching the optimal 0.5PZT-0.5MgO system observed in experiments (*21*). Low f limits polarized areas, reducing the maximum polarization P_m. On the other hand, high f diminishes FE/dielectric interfaces, weakening disordered relaxor characteristics and raising remnant polarization P_r, which in turn decreases U_e. Similarly, η is closely related to the relaxor nature, so η increases with reducing f (Fig. 3B). As a result, moderate f provides the best balance. We also noted plateau regions in U_e at higher fields for $f > 50\%$ and $x \sim 50$ to 60%, likely arising from effects of R/T-mixed phases, as explored later.

In contrast to the straightforward trends with f, variations in x reveal field-dependent optima. At low field (1 MV cm^{-1}), the highest U_e appears at $x \sim 90\%$ (T dominant). As fields rise, the optimal point shifts gradually to $x \sim 70\%$ (at 2 MV cm^{-1}), $x \sim 55\%$ (at 4 MV cm^{-1}), and finally $x \sim 50\%$ (at 8 MV cm^{-1}, R/T mixed). Meanwhile, the lowest η always occurs at high f and high x, while higher η starts at low f and high x for low field and then moves to low f and low x for high fields.

These variations of results, driving solely by varying x, highlight the critical roles of polymorphic phase engineering in dielectric energy storage. Apart from the orientations of polarization vectors, the key differences among the R-dominant, R/T-mixed, and T-dominant phases lie in their energy barriers for domain switching. From their energy landscapes (fig. S7), the T-dominant phase ($x = 70\%$) shows much deeper energy barriers for switching among their six variants. For the R-dominant phase ($x = 30\%$), the energy needed for switching is only about 40% of that in T-dominant phase, allowing easier rotations among eight variants. In the R/T-mixed phase, barriers for switching across all R and T variants drop further to roughly a quarter of the T-dominant phase, promoting more flexible rotations with fluctuating polarization distributions in both orientations and magnitudes.

We further examined the energy variations with varying Ti content x for $c = 3\%$ and $f = 50\%$ (fig. S8). The elastic and electrostatic energies show little changes for R-dominant, R/T-mixed, or T-dominant phases. The gradient energies increase with x, indicating higher domain wall energies in T-dominant phases, thereby suppressing nanodomain formation and weakening relaxor characteristics. The Landua free energy densities of R-dominant and R/T-mixed phases are comparable, while the T-dominant phase exhibits substantially lower Landau free energies due to its deeper energy barriers, consistent with their energy landscapes (fig. S7).

Building on these energy insights, we then chose four special cases of $x = 30$, 50, 70, and 90% at $f = 50\%$ for closer comparison of their effects on energy storage performance (Fig. 4A). The T-dominant phases yield higher U_e at relatively low fields (<2 MV cm^{-1}) but the T/R-mixed phase ($x = 50\%$) becomes advantageous at higher fields (≥4 MV cm^{-1}), with the gap widening. Eventually, the R/T-mixed phase achieves an U_e of 183 J cm^{-3} at 8 MV cm^{-1}, close to the experimental values ($U_e = 215.8$ J cm^{-3} at 7.4 MV cm^{-1}) (*21*). The discrepancies between the simulated and experimental results

Downloaded from https://www.science.org on February 20, 2026

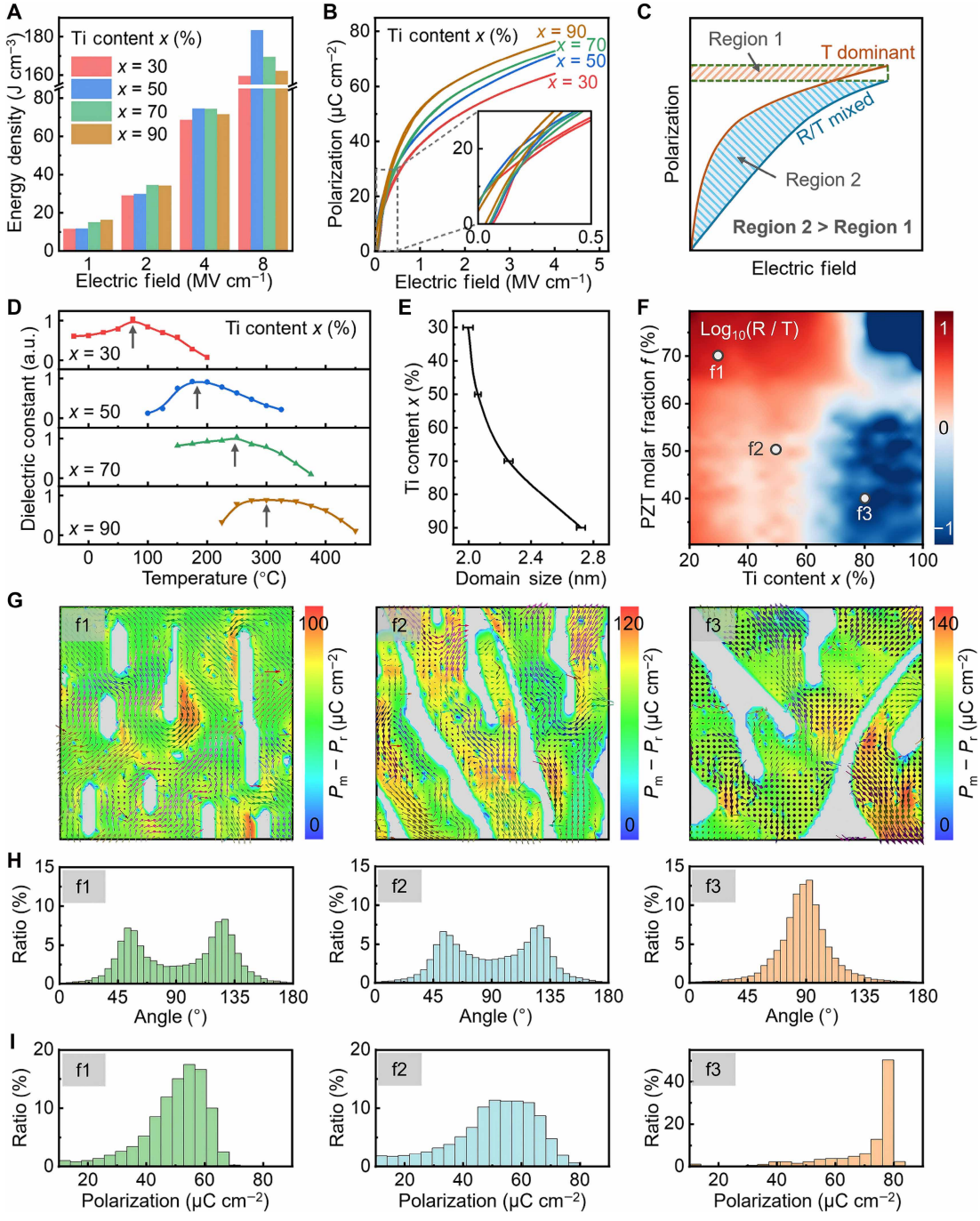

Fig. 4. Energy storage performance in PM systems with varying Ti content *x*. (**A**) Energy densities at different electric fields. (**B**) *P-E* loops at an electric field of 4 MV cm^{-1}. (**C**) Schematic comparison of energy density for T-dominant and R/T-mixed phases at a relatively high field. (**D**) Dielectric constants as a function of temperature. (**E**) Average domain sizes. (**F**) Map of R/T polarization ratios with respect to Ti contents and PZT molar fractions. (**G** to **I**) Comparison of (G) maps of local reversible polarizations and domain structures with areas of 32 nm by 32 nm, (H) histograms of polarization vector angles respect to the field direction, and (I) histograms of polarization vector magnitudes for three points marked in (F).

may stem from the two-dimensional nanostructure models and omitted complex defects or interfacial effects in the phase-field simulations. Since the experiments report ultrahigh breakdown fields (7.4 MV cm^{-1}) for these structures (*18*, *21*), we consider $E = 4$ MV cm^{-1} as a safe value in practical operations. From the *P-E* loops of different x at $f = 50\%$ and $E = 4$ MV cm^{-1} (Fig. 4B), we found that P_r remains similar across cases but P_m is larger with increasing x, so the reversible polarization ΔP follows the pattern that larger x shows higher ΔP throughout low to high fields (fig. S9). Note that the consistent P_r results mainly from the strong disordered effects through nanocomposite structures and defects. *P-E* loops without defects show the highest P_r at $x = 90\%$ and the lowest at $x = 50\%$, yielding

Downloaded from https://www.science.org on February 20, 2026

peak ΔP at $x = 50$ to 70% (fig. S10), highlighting the trade-off between P_m and P_r in R/T-mixed phases.

Clearly, the shift in optimal U_e from $x = 90\%$ to $x = 50\%$ with rising field goes beyond ΔP changes, linking to the *P-E* loop shapes, or specifically, the responses to fields during discharging process (from P_m to P_r). At low fields, the effective dielectric constant $|k_{eff}|$ for $x = 90\%$ exceeds others (fig. S11A), providing greater total polarization and U_e. Within this range, $|k_{eff}|$ is almost constant, so U_e is in proportion to ΔP (fig. S12). At higher fields, however, $|k_{eff}|$ reduces and nearly equalizes across compositions, making early low $|k_{eff}|$ (R/T mixed) beneficial instead because of its delayed saturation (Fig. 4C). This shifts the optimal x from T-dominant phase toward R/T mixtures as fields increase. At fields >2 MV cm^{-1}, where all cases reach near-saturation alignment, R/T-mixed phase indeed show a bit larger $|k_{eff}|$, further enhancing U_e, especially compared to $x = 90\%$ with the lowest $|k_{eff}|$ (fig. S11B). To explain these differences, we conducted dielectric constant calculations as a function of temperatures (Fig. 4D). The temperatures of peak response (T_m) for all cases are lower than those in the corresponding pure PZT (fig. S13), indicating reduced FE-paraelectric transition temperatures originating from weakened long-range order. T_m also drops with decreasing x, mirroring pure PZT trends and suggesting smaller domain sizes in R-dominant phases (*9*). This is verified by size statistics from ~2.7 nm for the T-dominant phase to <2.0 nm for the R-dominant one (Fig. 4E). The T-dominant phase exhibits larger domain sizes, which correlate with its higher switching barriers. Thus, it responds more strongly to applied fields due to stronger ferroelectricity and fewer disorders. In contrast, smaller nanodomains in R/T-mixed and R-dominant phases imply weaker FE interactions, leading to more uneven switching. Moreover, T domains can align fully with fields, whereas R domains retain nonaligned components despite comparable polarization magnitudes, which also contribute to the differences in P_m at the same field.

Beyond domain sizes, another way to gauge disorder is through variations in polarization vectors, including their orientations and magnitudes (*41*). Figure 4F maps R/T polarization ratios versus f and x. Note that a logarithmic scale is used, where 0 indicates equal R and T ratios, and 1 (or −1) means that R (or T) domains are 10 times the ratio of T (or R) domains. Equal ratios appear near x ~ 60%, slightly offset from pure PZT's MPB at x ~ 50% (fig. S1) because tilted branches in dendrite-like structures favor R phases to minimize depolarization effects. We then chose three representative points with R-dominant ($x = 30$ and $f = 70$), R/T-mixed ($x = 50$ and $f = 50$), and T-dominant ($x = 80$ and $f = 40$) phases. From their contour plots of the local reversible polarizations ΔP at an electric field of 4 MV cm^{-1} and corresponding domain patterns at zero field (Fig. 4G), we observed that in addition to regions with negative out-of-plane (OOP, direction of external fields) polarizations that naturally offer larger ΔP due to rotations more than 90°, the regions near R/T domain boundaries also enable more adaptable switching behaviors (Fig. 4G, middle), contributing to larger U_e. This phenomenon is largely observed in piezoelectric applications too (*33*, *35*), suggesting easier domain boundary motion from lower switching energies. Moreover, the distributions of polarization vectors for the three cases also show marked differences (Fig. 4, H and I). For the T-dominant phase, the orientations and magnitudes of local polarizations are quite narrow, indicating more regular domain patterns. Because the T-dominant phase shows higher energy barriers, or in other words, deeper energy well, it tends to generate larger domains and less domain walls to reduce high-level interim regions. For the R-dominant phase, in contrast, the polarizations display a much more dispersed distribution, mainly due to the lower barriers and smaller nanodomains. The R/T-mixed phase combines lowest barriers with easy transformation between the two phases, inducing fluctuating polarizations that respond to external fields in a more disordered manner, or in other words, contributing to its relaxor behaviors. Overall, for specific nanocomposite structures and electric fields, a balanced R/T ratio can effectively enhance relaxor behavior and promote energy storage performance.

To extend these insights to other relaxor systems, we further simulated a doped BNT-based system with defect engineering (note S2 and figs. S14 and S15). Energy densities at different electric fields (fig. S16) also show a field-dependent optima shifting from T-dominant phase at low fields to R/T-mixed phase at high fields, aligning with our primary results and underscoring the broad applicability of polymorphic phase engineering.

Stability of polymorphic phases

To assess the reliability of the polymorphic phase engineering, we evaluated energy storage performances under varying frequencies at 4 MV cm^{-1} (Fig. 5A). Because of limits in fitting kinetic coefficients in simulations, frequencies are in arbitrary units, with 1 a.u. matching the cases throughout this work. Over the range from 0.2 to 10 a.u., the R/T-mixed phase ($x = 50\%$) exhibits the highest stability, with energy density U_e variations <1.2% and efficiency η variations <4%. We ascribe its stability to the shallow energy barriers and small domain sizes that can react to fields quickly and independently. The R-dominant phase ($x = 30\%$) also performs well, with U_e variations <1.5% and η variations <5%. At higher frequencies, performance drops because of incomplete polarization responses to the applied field, resulting in elevated remnant polarization P_r. This decline becomes pronounced for T-dominant phases ($x = 90\%$), with U_e variations ~4.5% and η variations ~8.6%, owing to their higher switching barriers and larger domains slowing responses to rapid fields.

Similarly, temperature effects were also examined (Fig. 5B), revealing U_e and η variations <4% over a broad temperature range (−100° to 300°C), consistent with experiments (*21*). As temperature rises, U_e and η improve slightly across all x. The enhancement of performance is attributed to reduced ferroelectricity at elevated temperatures. This effect is similar to relaxor characteristics with enhanced local inhomogeneity and random fields (*9*), thus reducing P_r and domain sizes (fig. S17). We also mapped performances at $f = 50\%$ and $E = 4$ MV cm^{-1} with respect to temperature and Ti content x (Fig. 5, C and D), demonstrating robust thermal stability throughout. The optimal U_e occurs at x between 50 and 60%, and η increases with lower x, suggesting the best results in R/T-mixed phase. Note again that our phase-field model omits effects like leakage currents, potentially overestimating performance at high temperatures.

DISCUSSION

On the basis of the results, polymorphic phase engineering can be broadly applied to RFE systems for dielectric energy storage. In general, adding more T phases increases both the maximum polarization P_m and the remnant polarization P_r, due to their strong OOP polarization components and high energy barriers for switching. This makes T-dominant designs suitable for RFEs with very low P_r, allowing higher energy density U_e with minimal loss in efficiency η. It also works well at low electric fields because of their strong response to weak fields. However, T-dominant phases lack stability at

Downloaded from https://www.science.org on February 20, 2026

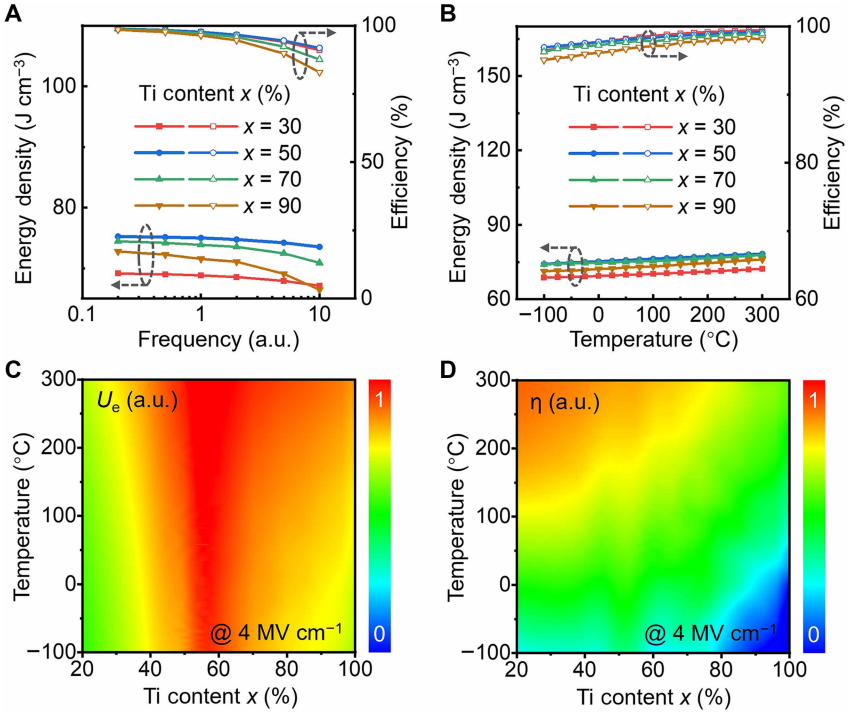

Fig. 5. Stability of energy storage performance. (**A** and **B**) Energy density and efficiency as a function of (A) frequency and (B) temperature for varying Ti contents. (**C** and **D**) Maps of (C) energy density and (D) efficiency with respect to temperature and Ti content.

high frequencies, restricting their use in demanding conditions. In contrast, R-dominant phases exhibit low P_r but also low P_m, which limits U_e despite high η from their smaller nanodomains. For polycrystalline or ceramic materials, however, the drawbacks of low OOP polarizations in R domains are lessened because of the random orientations of grains. Overall, R/T-mixed designs outperform single-phase ones in most scenarios, especially at higher fields. Polymorphic phases also provide the greatest stability across frequencies and temperatures. Nevertheless, our model omits complex factors such as leakage currents or interfacial effects. While this omission does not affect our core findings, it may lead to slightly higher predicted U_e and η at high fields or temperatures, where leakage could reduce performance because of increased dissipation. In addition, the simulations used two-dimensional dendrite-like nanocomposites, which might also differ slightly from actual three-dimensional ones.

In summary, through phase-field simulations, we systematically explored the effects and differences of phase designs, including R-dominant, R/T-mixed, and T-dominant phases, and their interplay with defects and dendrite-like nanocomposite structures in PM systems. We found that these dendrite-like structures, along with charged defects and defect dipoles, effectively break up long-range ordered polarizations and strengthen relaxor behaviors. Furthermore, we confirmed that the polymorphic design, e.g., R/T mixtures, can work synergistically with defects and nanostructures to further optimize energy density, efficiency, and stability, compared to single-phase cases, particularly under moderate to high fields. The benefits of polymorphic phases arise from their intrinsically low switching barriers, small nanoscale domains, and fluctuating polarization patterns. Our work establishes a theoretical basis for understanding polymorphic phases in dielectric energy storage and guiding the designs of advanced capacitors. Given the shared properties among mixed phases, our insights should apply universally to RFE designs in thin films or ceramics (*42*–*44*), and in materials ranging from Pb-based FEs such as rare earth–doped PZT (*30*) and PMN-PT (*45*) to Pb-free ones such as $BiFeO_3$-based (*24*, *46*), KNN-based (*47*), and BNT-based (*48*–*50*) systems.

MATERIALS AND METHODS

We used phase-field model to simulate the polarization evolutions of PMs. The polarization vector P_i ($i = 1, 2, 3$) is the order parameter. The total free energy (*51*) includes the densities of Landau free energy f_{Land}, gradient energy f_{grad}, elastic energy f_{elas}, and electrostatic energy term f_{elec}

$$F = \int_V \left(f_{Land} + f_{grad} + f_{elas} + f_{elec}\right) dV \tag{1}$$

The Landau free energy density is

$$\begin{aligned} f_{Land} = {} & \alpha_1\left(P_1^2 + P_2^2 + P_3^2\right) + \alpha_{11}\left(P_1^4 + P_2^4 + P_3^4\right) \\ & + \alpha_{12}\left(P_1^2P_2^2 + P_2^2P_3^2 + P_3^2P_1^2\right) + \alpha_{111}\left(P_1^6 + P_2^6 + P_3^6\right) \\ & + \alpha_{12}\left[P_1^2\left(P_2^4 + P_3^4\right) + P_2^2\left(P_3^4 + P_1^4\right) + P_3^2\left(P_1^4 + P_2^4\right)\right] \\ & + \alpha_{123}P_1^2P_2^2P_3^2 \end{aligned} \tag{2}$$

where α_1, α_{11}, α_{12}, α_{111}, α_{112}, and α_{123} are the Landau polynomial coefficients. The gradient energy density is

$$f_{grad} = \frac{1}{2}g_{11}\left(P_{1,1}^2 + P_{2,2}^2 + P_{3,3}^2 + P_{1,2}^2 + P_{2,1}^2 + P_{1,3}^2 + P_{3,1}^2 + P_{2,3}^2 + P_{3,2}^2\right) \tag{3}$$

Downloaded from https://www.science.org on February 20, 2026

where g_{11} is the isotropic gradient energy coefficient, and $P_{i,j}$ denotes $\partial P_i/\partial x_j$ with x_j as the spatial coordinate. The elastic energy density is

$$f_{\text{elas}} = \frac{1}{2}c_{ijkl}\left(\varepsilon_{ij}-\varepsilon^0_{ij}\right)\left(\varepsilon_{kl}-\varepsilon^0_{kl}\right) \quad (4)$$

where c_{ijkl} is the elastic stiffness tensor, ε_{ij} and $\varepsilon^0{}_{ij} = Q_{ijkl}P_kP_l$ are the total strain and eigenstrain, respectively, with Q_{ijkl} as the electrostrictive coefficients. The electrostatic energy density is

$$f_{\text{elec}} = -E_iP_i - \frac{1}{2}\varepsilon_0\kappa^{\text{b}}E_iE_i \quad (5)$$

where $E_i = -\partial\varphi/\partial x_i$ is the electric field with φ as the electrostatic potential, ε_0 and κ^{b} are the permittivity of vacuum and the background relative dielectric constant, respectively.

The temporal evolution of polarizations was calculated by the time-dependent Ginzburg-Landau equations

$$\frac{\partial P_i}{\partial t} = -L_{\text{P}}\frac{\delta F}{\delta P_i} \quad (6)$$

where L_P is the kinetic coefficient, and the semi-implicit Fourier spectral method was used (*52*). The elastic and electrical parameters were solved by the spectral iterative perturbation method (*53*) from the mechanical equilibrium equations $\sigma_{ij,j} = 0$ and the electrostatic equilibrium equation $D_{i,i} = 0$, where the local stress $\sigma_{ij} = c_{ijkl}(\varepsilon_{ij} - \varepsilon^0{}_{ij})$ and the electric displacement $D_i = \varepsilon_0\kappa^{\text{b}}E_i + P_i$. Bound charges, arising from polarization discontinuities, generate depolarization fields that are resolved via electrostatic equilibrium equations. The stress-free boundary conditions and reduced PM lattice mismatches of 3% are used to account for elastic effects from defects such as dislocations.

The PM systems are a mixture of PZT regions, MgO regions. and boundary regions, distinguished by the coefficients. For PZT, the coefficients, according to previous literature (*54*, *55*), vary with Ti content x as (in SI units)

$$\alpha_1 = \left(T-T_0\right)/\left(2\times 8.85\times 10^{-12}\times C_0\right),$$
$$\alpha_{11} = \left(10.612-22.655x+10.955x^2\right)\times 10^{13}/C_0,$$
$$\alpha_{12} = \eta_1/3-\alpha_{11},$$
$$\alpha_{111} = \left(12.026-17.296x+9.179x^2\right)\times 10^{13}/C_0,$$
$$\alpha_{112} = \left(4.2904-3.3754x+58.804e^{-29.397x}\right)\times 10^{14}/C_0,$$
$$\alpha_{123} = \eta_2-3\alpha_{111}-6\alpha_{112},$$
$$\eta_1 = \left[2.6213+0.42743x-(9.6+0.012501x)e^{-12.6x}\right]\times 10^{14}/C_0,$$
$$\eta_2 = \left[0.887+0.76973x-(16.225-0.088651x)e^{-21.255x}\right]\times 10^{15}/C_0,$$
$$T_0 = 462.63+843.4x-2105.5x^2+4041.8x^3-3828.3x^4+1337.8x^5,$$
$$C_0 = \begin{cases}\left[\dfrac{2.1716}{1+500.05(x-0.5)^2}+0.131x+2.01\right]\times 10^5, & \text{when } x\le 0.5,\\ \left[\dfrac{2.8339}{1+126.56(x-0.5)^2}+1.4132\right]\times 10^5, & \text{when } x>1.0,\end{cases}$$
$$Q_{11} = \frac{0.029578}{1+200(x-0.5)^2}+0.042796x+0.045624,$$
$$Q_{12} = -\frac{0.026568}{1+200(x-0.5)^2}-0.012093x-0.013386,$$
$$Q_{44} = \frac{0.025325}{1+200(x-0.5)^2}+0.020857x+0.046147$$

Meanwhile, c_{11} = 168 GPa, c_{12} = 83 GPa, c_{44} = 41 GPa for $x \le 0.45$; c_{11} = 154 GPa, c_{12} = 84 GPa, c_{44} = 35 GPa for $0.45 < x \le 0.55$; c_{11} = 170 GPa, c_{12} = 82 GPa, c_{44} = 47 GPa for $0.55 < x \le 0.65$; c_{11} = 171 GPa, c_{12} = 81 GPa, c_{44} = 57 GPa for $0.65 < x \le 0.75$; c_{11} = 173 GPa, c_{12} = 80 GPa, c_{44} = 69 GPa for $0.75 < x \le 0.85$; c_{11} = 170 GPa, c_{12} = 76 GPa, c_{44} = 83 GPa for $0.85 < x \le 0.95$; c_{11} = 175 GPa, c_{12} = 79 GPa, c_{44} = 111 GPa for $x > 0.95$, and $\kappa_b = 40$. For MgO, $\alpha_1 = 5.650\times 10^9$ C^{-2} m ^{2}N, $\alpha_{11} = \alpha_{12} = \alpha_{111} = \alpha_{112} = \alpha_{123} = 0$, c_{11} = 293 GPa, c_{12} = 92 GPa, c_{44} = 155 GPa, and κ_b = 10. For boundaries between PZT and MgO, the coefficients are the average of these of PZT and MgO. The gradient energy coefficient $g_{11} = 2.987\times 10^{-11}$ C^{-2} m ^{4}N. The whole system grid is $256\Delta x \times 1\Delta x \times 256\Delta x$ with Δx = 0.4 nm, and the periodic boundary conditions were adopted.

To simulate defects, we randomly added point charges on the boundaries and pinning dipoles within PZT regions. The charges obey a normal distribution of mean $\mu = \pm 2.5\times 10^9$ C/m^3 (~1 e/u.c.) and SD σ = 0.1 μ. The pinning dipoles were assumed to be O phases with magnitudes obeying a normal distribution of mean μ = 0.7 C/m^2 and SD σ = 0.1 μ.

Supplementary Materials

This PDF file includes:

Supplementary Notes S1 and S2
Figs. S1 to S17
References

REFERENCES

1. B. Chu, X. Zhou, K. Ren, B. Neese, M. Lin, Q. Wang, F. Bauer, Q. M. Zhang, A dielectric polymer with high electric energy density and fast discharge speed. *Science* **313**, 334–336 (2006).
2. Q. Li, L. Chen, M. R. Gadinski, S. Zhang, G. Zhang, H. Li, E. Iagodkine, A. Haque, L.-Q. Chen, T. Jackson, Q. Wang, Flexible high–temperature dielectric materials from polymer nanocomposites. *Nature* **523**, 576–579 (2015).
3. H. Palneedi, M. Peddigari, G.-T. Hwang, D.-Y. Jeong, J. Ryu, High-performance dielectric ceramic films for energy storage capacitors: Progress and outlook. *Adv. Funct. Mater.* **28**, 1803665 (2018).
4. H. Pan, F. Li, Y. Liu, Q. Zhang, M. Wang, S. Lan, Y. Zheng, J. Ma, L. Gu, Y. Shen, P. Yu, S. Zhang, L.-Q. Chen, Y.-H. Lin, C.-W. Nan, Ultrahigh–energy density lead-free dielectric films via polymorphic nanodomain design. *Science* **365**, 578–582 (2019).
5. G. Wang, Z. Lu, Y. Li, L. Li, H. Ji, A. Feteira, D. Zhou, D. Wang, S. Zhang, I. M. Reaney, Electroceramics for high-energy density capacitors: Current status and future perspectives. *Chem. Rev.* **121**, 6124–6172 (2021).
6. Y. Liu, B. Yang, S. Lan, H. Pan, C.-W. Nan, Y.-H. Lin, Perspectives on domain engineering for dielectric energy storage thin films. *Appl. Phys. Lett.* **120**, 150501 (2022).
7. Y. Zhang, L. Chen, H. Liu, S. Deng, H. Qi, J. Chen, High-performance ferroelectric based materials via high-entropy strategy: Design, properties, and mechanism. *InfoMat* **5**, e12488 (2023).
8. F. Li, S. Zhang, D. Damjanovic, L.-Q. Chen, T. R. Shrout, Local structural heterogeneity and electromechanical responses of ferroelectrics: Learning from relaxor ferroelectrics. *Adv. Funct. Mater.* **28**, 1801504 (2018).
9. Y. Liu, B. Yang, S. Lan, Z. Zhou, L. Dou, C.-W. Nan, Y.-H. Lin, Harnessing local inhomogeneity for enhanced dielectric energy storage. *Nat. Commun.* **16**, 6236 (2025).
10. V. Polinger, I. B. Bersuker, Origin of polar nanoregions and relaxor properties of ferroelectrics. *Phys. Rev. B* **98**, 214102 (2018).
11. X. Shi, J. Wang, J. Xu, X. Cheng, H. Huang, Quantitative investigation of polar nanoregion size effects in relaxor ferroelectrics. *Acta Mater.* **237**, 118147 (2022).
12. L. Shu, X. Shi, X. Zhang, Z. Yang, W. Li, Y. Ma, Y.-X. Liu, L. Liu, Y.-Y.-S. Cheng, L. Wei, Q. Li, H. Huang, S. Zhang, J.-F. Li, Partitioning polar–slush strategy in relaxors leads to large energy–storage capability. *Science* **385**, 204–209 (2024).

Downloaded from https://www.science.org on February 20, 2026

13. H. Tao, H. Wu, Y. Liu, Y. Zhang, J. Wu, F. Li, X. Lyu, C. Zhao, D. Xiao, J. Zhu, S. J. Pennycook, Ultrahigh performance in lead-free piezoceramics utilizing a relaxor slush polar state with multiphase coexistence. *J. Am. Chem. Soc.* **141**, 13987–13994 (2019).
14. M. Zhang, S. Lan, B. B. Yang, H. Pan, Y. Q. Liu, Q. H. Zhang, J. L. Qi, D. Chen, H. Su, D. Yi, Y. Y. Yang, R. Wei, H. D. Cai, H. J. Han, L. Gu, C.-W. Nan, Y.-H. Lin, Ultrahigh energy storage in high-entropy ceramic capacitors with polymorphic relaxor phase. *Science* **384**, 185–189 (2024).
15. B. Yang, Y. Zhang, H. Pan, W. Si, Q. Zhang, Z. Shen, Y. Yu, S. Lan, F. Meng, Y. Liu, H. Huang, J. He, L. Gu, S. Zhang, L.-Q. Chen, J. Zhu, C.-W. Nan, Y.-H. Lin, High-entropy enhanced capacitive energy storage. *Nat. Mater.* **21**, 1074–1080 (2022).
16. J. Kim, S. Saremi, M. Acharya, G. Velarde, E. Parsonnet, P. Donahue, A. Qualls, D. Garcia, L. W. Martin, Ultrahigh capacitive energy density in ion-bombarded relaxor ferroelectric films. *Science* **369**, 81–84 (2020).
17. H. Pan, N. Feng, X. Xu, W. Li, Q. Zhang, S. Lan, Y.-Q. Liu, H. Sha, K. Bi, B. Xu, J. Ma, L. Gu, R. Yu, Y. Shen, X. R. Wang, J. L. MacManus-Driscoll, C.-L. Chen, C.-W. Nan, Y.-H. Lin, Enhanced electric resistivity and dielectric energy storage by vacancy defect complex. *Energy Storage Mater.* **42**, 836–844 (2021).
18. Y. Liu, M. Li, K. Jiang, Y. Zhang, P. Gong, S. Song, D. Li, H. Liang, X. Huang, J. Wang, W. Li, C.-W. Nan, Radiation-hardened dendritic-like nanocomposite films with ultrahigh capacitive energy density. *Nat. Commun.* **16**, 3882 (2025).
19. S. Han, J. S. Kim, E. Park, Y. Meng, Z. Xu, A. C. Foucher, G. Y. Jung, I. Roh, S. Lee, S. O. Kim, J.-Y. Moon, S.-I. Kim, S. Bae, X. Zhang, B.-I. Park, S. Seo, Y. Li, H. Shin, K. Reidy, A. T. Hoang, S. Sundaram, P. Vuong, C. Kim, J. Zhao, J. Hwang, C. Wang, H. Choi, D.-H. Kim, J. Kwon, J.-H. Park, A. Ougazzaden, J.-H. Lee, J.-H. Ahn, J. Kim, R. Mishra, H.-S. Kim, F. M. Ross, S.-H. Bae, High energy density in artificial heterostructures through relaxation time modulation. *Science* **384**, 312–317 (2024).
20. S. S. Cheema, N. Shanker, S.-L. Hsu, J. Schaadt, N. M. Ellis, M. Cook, R. Rastogi, R. C. N. Pilawa-Podgurski, J. Ciston, M. Mohamed, S. Salahuddin, Giant energy storage and power density negative capacitance superlattices. *Nature* **629**, 803–809 (2024).
21. Y. Liu, Y. Zhang, J. Wang, C. Yang, H. Wang, J. L. MacManus-Driscoll, H. Yang, P. A. van Aken, W. Li, C.-W. Nan, Ultrahigh capacitive energy storage through dendritic nanopolar design. *Science* **388**, 211–216 (2025).
22. R. Lu, J. Wang, T. Duan, T.-Y. Hu, G. Hu, Y. Liu, W. Fu, Q. Han, Y. Lu, L. Lu, S.-D. Cheng, Y. Dai, D. Hu, Z. Shen, C.-L. Jia, C. Ma, M. Liu, Metadielectrics for high-temperature energy storage capacitors. *Nat. Commun.* **15**, 6596 (2024).
23. H. Aramberri, N. S. Fedorova, J. Íñiguez, Ferroelectric/paraelectric superlattices for energy storage. *Sci. Adv.* **8**, eabn4880 (2022).
24. H. Pan, Y. Zeng, Y. Shen, Y.-H. Lin, J. Ma, L. Li, C.-W. Nan, $BiFeO_3$–$SrTiO_3$ thin film as a new lead-free relaxor-ferroelectric capacitor with ultrahigh energy storage performance. *J. Mater. Chem. A* **5**, 5920–5926 (2017).
25. H. Pan, S. Lan, S. Xu, Q. Zhang, H. Yao, Y. Liu, F. Meng, E.-J. Guo, L. Gu, D. Yi, X. Renshaw Wang, H. Huang, J. L. MacManus-Driscoll, L.-Q. Chen, K.-J. Jin, C.-W. Nan, Y.-H. Lin, Ultrahigh energy storage in superparaelectric relaxor ferroelectrics. *Science* **374**, 100–104 (2021).
26. C. Li, Y. Liu, B. Li, Z. Yuan, T. Yang, Y. Liu, H. Gao, L. Xu, X. Yu, Q. Luo, S. Tang, M. Yao, Y. Gong, Z. Fei, L.-Q. Chen, H. Zhang, H. Zhou, Q. Wang, Enhanced energy storage in high-entropy ferroelectric polymers. *Nat. Mater.* **24**, 1066–1073 (2025).
27. B. Yang, Y. Liu, C. Gong, S. Lan, Z. Zhou, X. Zhu, C.-W. Nan, Y.-H. Lin, Design of high-entropy relaxor ferroelectrics for comprehensive energy storage enhancement. *Adv. Funct. Mater.* **34**, 2409344 (2024).
28. B. Yang, Q. Zhang, H. Huang, H. Pan, W. Zhu, F. Meng, S. Lan, Y. Liu, B. Wei, Y. Liu, L. Yang, L. Gu, L.-Q. Chen, C.-W. Nan, Y.-H. Lin, Engineering relaxors by entropy for high energy storage performance. *Nat. Energy* **8**, 956–964 (2023).
29. S. Saremi, R. Xu, L. R. Dedon, J. A. Mundy, S. Hsu, Z. Chen, A. R. Damodaran, S. P. Chapman, J. T. Evans, L. W. Martin, Enhanced electrical resistivity and properties via ion bombardment of ferroelectric thin films. *Adv. Mater.* **28**, 10750–10756 (2016).
30. M. D. Nguyen, Y. A. Birkhölzer, E. P. Houwman, G. Koster, G. Rijnders, Enhancing the energy-storage density and breakdown strength in $PbZrO_3$/$Pb_{0.9}La_{0.1}Zr_{0.52}Ti_{0.48}O_3$-derived antiferroelectric/relaxor-ferroelectric multilayers. *Adv. Energy Mater.* **12**, 2200517 (2022).
31. B. Yang, Y. Liu, W. Li, S. Lan, L. Dou, X. Zhu, Q. Li, C.-W. Nan, Y.-H. Lin, Balancing polarization and breakdown for high capacitive energy storage by microstructure design. *Adv. Mater.* **36**, e2403400 (2024).
32. F. Li, M. J. Cabral, B. Xu, Z. Cheng, E. C. Dickey, J. M. LeBeau, J. Wang, J. Luo, S. Taylor, W. Hackenberger, L. Bellaiche, Z. Xu, L.-Q. Chen, T. R. Shrout, S. Zhang, Giant piezoelectricity of Sm-doped $Pb(Mg_{1/3}Nb_{2/3})O_3$–$PbTiO_3$ single crystals. *Science* **364**, 264–268 (2019).
33. Y. Cao, G. Sheng, J. X. Zhang, S. Choudhury, Y. L. Li, C. A. Randall, L. Q. Chen, Piezoelectric response of single-crystal $PbZr_{1-x}Ti_xO_3$ near morphotropic phase boundary predicted by phase-field simulation. *Appl. Phys. Lett.* **97**, 252904 (2010).
34. X. Lv, J. Zhu, D. Xiao, X. Zhang, J. Wu, Emerging new phase boundary in potassium sodium-niobate based ceramics. *Chem. Soc. Rev.* **49**, 671–707 (2020).
35. F. Cordero, Elastic properties and enhanced piezoelectric response at morphotropic phase boundaries. *Materials* **8**, 8195–8245 (2015).
36. Y. Liu, J. Liu, H. Pan, X. Cheng, Z. Hong, B. Xu, L.-Q. Chen, C.-W. Nan, Y.-H. Lin, Phase-field simulations of tunable polar topologies in lead-free ferroelectric/paraelectric multilayers with ultrahigh energy-storage performance. *Adv. Mater.* **34**, 2108772 (2022).
37. Z. Shen, J. Wang, Y. Lin, C. Nan, L. Chen, Y. Shen, High-throughput phase-field design of high-energy-density polymer nanocomposites. *Adv. Mater.* **30**, 1704380 (2018).
38. X. Chen, Z.-H. Shen, R.-L. Liu, Y. Shen, H.-X. Liu, L.-Q. Chen, C.-W. Nan, Programming polarity heterogeneity of energy storage dielectrics by bidirectional intelligent design. *Adv. Mater.* **36**, 2311721 (2024).
39. K. Xu, L. Yang, J. Wang, H. Huang, Design of high energy storage ferroelectric materials by phase-field simulations. *J. Mater. Inform.* **5**, 24 (2025).
40. R. Kobayashi, Modeling and numerical simulations of dendritic crystal growth. *Phys. D* **63**, 410–423 (1993).
41. Y. Yao, H. Liu, Y. Hu, K. Datta, J. Wu, Y. Zhang, M. G. Tucker, S. Liu, J. C. Neuefeind, S. Zhang, J. Chen, Fluctuating local polarization: A generic fingerprint for enhanced piezoelectricity in Pb-based and Pb-free perovskite ferroelectrics. *Nat. Commun.* **16**, 7442 (2025).
42. Y. Ren, H. Cheng, J. Ouyang, O. Kurt, J. Wang, Q. Zhang, Y. Zhao, L. Gu, L.-Q. Chen, Bimodal polymorphic nanodomains in ferroelectric films for giant energy storage. *Energy Storage Mater.* **48**, 306–313 (2022).
43. A. Xie, Z. Yu, J. Lei, Y. Zhang, A. Tian, X. Jiang, X. Xie, Y. Yin, Z. Fu, X. Li, R. Zuo, Superior capacitive energy storage of $BaTiO_3$-based polymorphic relaxor ferroelectrics engineered by mesoscopically chemical homogeneity. *Adv. Sci.* **12**, e2502916 (2025).
44. Y. Zheng, W. Liu, A. Xie, Q. Jiang, Z. Li, X. Wu, A. Tian, Y. Zhang, X. Jiang, R. Zuo, Ultrahigh energy-storage performance under moderate fields in $BiFeO_3$-$BaTiO_3$-based ceramics via domain and band-gap modulation. *Ceram. Int.* **51**, 39238–39246 (2025).
45. T. F. Zhang, X. G. Tang, Q. X. Liu, Y. P. Jiang, X. X. Huang, Q. F. Zhou, Energy-storage properties and high-temperature dielectric relaxation behaviors of relaxor ferroelectric $Pb(Mg_{1/3}Nb_{2/3})O_3$–$PbTiO_3$ ceramics. *J. Phys. D: Appl. Phys.* **49**, 095302 (2016).
46. H. Pan, J. Ma, J. Ma, Q. Zhang, X. Liu, B. Guan, L. Gu, X. Zhang, Y.-J. Zhang, L. Li, Y. Shen, Y.-H. Lin, C.-W. Nan, Giant energy density and high efficiency achieved in bismuth ferrite-based film capacitors via domain engineering. *Nat. Commun.* **9**, 1813 (2018).
47. Q. Chai, F. Zhang, Q. Zhou, Z. Peng, D. Wu, P. Liang, L. Wei, X. Chao, Z. Yang, Superior energy storage properties and optical transparency in $K_{0.5}Na_{0.5}NbO_3$-based dielectric ceramics via multiple synergistic strategies. *Small* **19**, 2207464 (2023).
48. H. Ji, D. Wang, W. Bao, Z. Lu, G. Wang, H. Yang, A. Mostaed, L. Li, A. Feteira, S. Sun, F. Xu, D. Li, C.-J. Ma, S.-Y. Liu, I. M. Reaney, Ultrahigh energy density in short-range tilted NBT-based lead-free multilayer ceramic capacitors by nanodomain percolation. *Energy Storage Mater.* **38**, 113–120 (2021).
49. W. Zhu, Z.-Y. Shen, W. Deng, K. Li, W. Luo, F. Song, X. Zeng, Z. Wang, Y. Li, A review: (Bi,Na)TiO_3 (BNT)-based energy storage ceramics. *J. Materiomics* **10**, 86–123 (2024).
50. W. Zhao, Z. Liu, D. Xu, G. Wang, D. Li, J. Liu, Z. Wang, Y. Guo, J. Ren, T. Zhou, L. Pang, H. Yang, W. Liu, H. Huang, D. Zhou, Advanced stability and energy storage capacity in hierarchically engineered $Bi_{0.5}Na_{0.5}TiO_3$-based multilayer capacitors. *Nat. Commun.* **16**, 6549 (2025).
51. L.-Q. Chen, Phase-field models for microstructure evolution. *Annu. Rev. Mater. Res.* **32**, 113–140 (2002).
52. L. Q. Chen, J. Shen, Applications of semi-implicit fourier-spectral method to phase field equations. *Comput. Phys. Commun.* **108**, 147–158 (1998).
53. J. J. Wang, X. Q. Ma, Q. Li, J. Britson, L.-Q. Chen, Phase transitions and domain structures of ferroelectric nanoparticles: Phase field model incorporating strong elastic and dielectric inhomogeneity. *Acta Mater.* **61**, 7591–7603 (2013).
54. L.-Q. Chen, "APPENDIX A –Landau free-energy coefficients" in *Physics of Ferroelectrics: A Modern Perspective* (Springer, 2007), pp. 363–372. https://doi.org/10.1007/978-3-540-34591-6_9.
55. M. J. Haun, E. Furman, Z. Q. Zhuang, S. J. Jang, L. E. Cross, Thermodynamic theory of the lead zirconate-titanate solid solution system. *Ferroelectrics* **94**, 313–313 (1989).
56. X. Q. Ke, D. Wang, X. Ren, Y. Wang, Formation of monoclinic nanodomains at the morphotropic phase boundary of ferroelectric systems. *Phys. Rev. B* **88**, 214105 (2013).
57. J. Yin, X. Shi, H. Tao, Z. Tan, X. Lv, X. Ding, J. Sun, Y. Zhang, X. Zhang, K. Yao, J. Zhu, H. Huang, H. Wu, S. Zhang, J. Wu, Deciphering the atomic-scale structural origin for large dynamic electromechanical response in lead-free $Bi_{0.5}Na_{0.5}TiO_3$-based relaxor ferroelectrics. *Nat. Commun.* **13**, 6333 (2022).

Acknowledgments: The authors also acknowledge Beijng PARATERA Tech CO., Ltd. for providing HPC resources that have contributed to the researh results reported within this paper (https://www.paratera.com/). **Funding:** This work was supported by the National Natural Science Foundation of China (NSFC) grants 92477107 (W.-W.L.), 52302184 (Y.Z.), and 52472125 (J.W.); the Basic Science Center Project of the National Natural Science Foundation of China (NSFC) grant 52388201 (C.-W.N.); the National Natural Science Foundation of Jiangsu Province grant BK20250078 (W.-W.L.); the open research fund of Key Laboratory of Quantum Materials and Devices (Southeast University), Ministry of Education (Y.Z.); the Research Fund of State Key Laboratory of Mechanics and Control for Aerospace Structures (Nanjing University of Aeronautics

Downloaded from https://www.science.org on February 20, 2026

and Astronautics) grants MCAS-I-0424G02 and MCAS-I-0525 K01 (W.-W.L.); the Fundamental Research Funds for the Central Universities grants NE2025009, NS2023057, and NI2023001 (W.-W.L.); the Research Fund for Stable Support for Basic Research Projects of National Defense Characteristics grant ILF240031A24 (W.-W.L.); the Top-notch Academic Programs Project of Jiangsu Higher Education Institutions (TAPP) (W.-W.L.); the Postdoctoral Fellowship Program and China Postdoctoral Science Foundation grants BX20250450 and 2025M784318 (Y.L); and the Jiangsu Funding Program for Excellent Postdoctoral Talent grants 2025ZB43 (Y.L.). **Author contributions:** W.-W.L. conceived and supervised this study. Y.Z. performed the phase-field simulations with the help from H.L., Y.L., D.L., S.D. Y.Z., J.W., W.-W.L., and C.-W.N. wrote the draft of the manuscript. All authors discussed the results and revised the manuscript. **Competing interests:** The authors declare that they have no competing interests. **Data, code, and materials availability:** All data and code needed to evaluate and reproduce the results in the paper are present in the paper and/or the Supplementary Materials. This study did not generate new materials.

Submitted 24 August 2025
Accepted 15 January 2026
Published 20 February 2026
10.1126/sciadv.aeb7173

Downloaded from https://www.science.org on February 20, 2026